LAWRENCE
LIVERMORE
NATIONAL
LABORATORY

LLNL-TR-706674

Acoustic Wave Propagation Modeling by a Two-dimensional Finite-difference Summation-by-parts Algorithm

K. Kim, N. A. Petersson, A. Rodgers

October 25, 2016

Disclaimer

This work performed under the auspices of the U.S. Department of Energy by Lawrence Livermore National Laboratory under Contract DE-AC52-07NA27344.

Acoustic wave propagation modeling by a 2-D finite-difference summation-by-parts algorithm

K. Kim, N. A. Petersson, and A. Rodgers
Lawrence Livermore National Laboratory, Livermore, California, USA.

Abstract

Acoustic waveform modeling is a computationally intensive task and full three-dimensional simulations are often impractical for some geophysical applications such as long-range wave propagation and high-frequency sound simulation. In this study, we develop a two-dimensional high-order accurate finite-difference code for acoustic wave modeling. We solve the linearized Euler equations by discretizing them with the sixth order accurate finite difference stencils away from the boundary and the third order summation-by-parts (SBP) closure near the boundary. Non-planar topographic boundary is resolved by formulating the governing equation in curvilinear coordinates following the interface. We verify the implementation of the algorithm by numerical examples and demonstrate the capability of the proposed method for practical acoustic wave propagation problems in the atmosphere.

1. Introduction

Natural and/or man-made explosions near the earth's surface radiate significant energies into the atmosphere in the form of acoustic waves. Accurate modeling of acoustic wave propagation in the atmosphere is important in explosion forensics for event identification [*Walker et al.*, 2011; *Park et al.*, 2014; *Kim and Lees*, 2014] and characterization such as explosion yield and height of burst [*Bonner et al.*, 2013; *Ford et al.*, 2014; *Kim and Rodgers*, 2016]. LLNL developed the full three-dimensional elasto-acoustic simulation code, called ElAc [*Sjogreen and Petersson*, 2016], providing accurate seismic and acoustic wave modeling capabilities. ElAc uses finite-difference summation-by-parts algorithm to solve the linearized Euler equations in the atmosphere and seismic wave equations in the solid earth and take into account the coupling of seismic and acoustic waves near the earth's surface, providing a unique capability to simulate seismo-acoustic wavefields simultaneously [*Petersson and Sjogreen*, 2016].

However, ElAc's capability for acoustic wave modeling may be practically limited by computational performance. The finite-difference spatial discretization in ElAc requires at

least 10 grid points per the shortest wavelength to resolve the wave modes and acquire the desired accuracy. The speed of sound in the atmosphere generally varies with altitudes in 270 – 350m/s [*NOAA*, 1976]. For $\sim$ 0.5Hz acoustic waves, which is expected to be observed at $\sim$ 300km from an 8kt nuclear explosion [*Gainville et al.*, 2009], a full 3-D ElAc simulation of acoustic propagation out to 300km will require a large amount of computer memory to store finite-difference grid cells more than ten billion. In addition, this requirement significantly increases computation time and restricts the size of acoustic domain, and therefore ElAc may not be practical for long-range and/or high-frequency acoustic wave propagation which often arise in geophysical problems.

In this study, we develop a 2-D acoustic wave simulation code using the same finite-difference summation-by-parts algorithm used in 3-D ElAc. Instead of using full 3-D equations, we solve the 2-D linearized Euler equations and which reduces computational workload substantially compared to the 3-D case. Therefore, the 2-D solver can be used to compute approximated acoustic solutions when full 3-D simulation is not practical.

This report is organized as follows. In Section 2 we explain the numerical method used in the code. The 2-D governing equations and their discretized formulations are presented. In order to resolve non-planar topographic boundary, the equations are formulated in a curvilinear grid that follows the boundary. In Section 3 we verify the correctness of numerical implementation by the method of manufactured solutions. And then numerical examples are provided, which demonstrate the capability of the 2-D acoustic solver for sound propagation simulation in a moving atmosphere.

2. Method

This section focuses on the finite-difference formulation for the governing equations. We follows the same approach proposed by *Petersson and Sjogreen* [2016] and briefly review them here for the completeness of this report. Readers interested in detailed development of the approach are referred to *Petersson and Sjogreen* [2016].

2.1. Linearized Euler Equations

The 2-D linearized Euler equations for compressible fluid flow is used to model acoustic wave propagation in a moving atmosphere, and the equations are symmetrized as follows:

$$\mathbf{q}_t + A\partial_1\mathbf{q} + B\partial_2\mathbf{q} + E\mathbf{q} = \mathbf{f}, \tag{1}$$

where partial differentiation with respect to Cartesian coordinates is denoted by $\partial_k = \partial/\partial x_k$, and temporal differentiation is written by $\partial_t = \partial/\partial t$. The dependent variables are $\mathbf{q} = (s, u, v, r)^T$, where $\mathbf{u} = (u, v)^T$ is perturbed particle velocities in $\mathbf{x_1}$ and $\mathbf{x_2}$ directions. In addition, ambient parameters for the pressure, density, and medium velocity will be denoted by $\hat{p}, \hat{\rho}$, and $\hat{\mathbf{u}} = (\hat{u}, \hat{v})^T$, respectively. The variables s and r are defined by overpressure p

and density perturbation ρ as

$$s = \frac{1}{\sqrt{\gamma}} \frac{\hat{c}}{\hat{\rho}}, \tag{2}$$

$$r = -1 \frac{1}{\sqrt{\gamma(\gamma-1)}} \frac{\hat{c}}{\hat{\rho}} \rho + \frac{\sqrt{\gamma}}{\sqrt{\gamma-1}} \frac{1}{\hat{\rho}\hat{c}} p. \tag{3}$$

Here, $\hat{c} = \sqrt{\gamma \hat{p}/\hat{\rho}}$ is the speed of sound in the medium and $\gamma > 1$ is the ratio of specific heats. A and B are the symmetric matrices that satisfy

$$A = \begin{pmatrix} \hat{u} & \frac{1}{\sqrt{\gamma}} & 0 & 0 \\ \frac{1}{\sqrt{\gamma}} & \hat{u} & 0 & \sqrt{\frac{\gamma-1}{\gamma}}\hat{c} \\ 0 & 0 & \hat{u} & 0 \\ 0 & \sqrt{\frac{\gamma-1}{\gamma}}\hat{c} & 0 & \hat{u} \end{pmatrix}, \quad B = \begin{pmatrix} \hat{v} & 0 & \frac{1}{\sqrt{\gamma}} & 0 \\ 0 & \hat{v} & 0 & 0 \\ \frac{1}{\sqrt{\gamma}} & 0 & \hat{v} & \sqrt{\frac{\gamma-1}{\gamma}}\hat{c} \\ 0 & 0 & \sqrt{\frac{\gamma-1}{\gamma}}\hat{c} & \hat{v} \end{pmatrix}. \tag{4}$$

The matrix E is given by

$$E = \begin{pmatrix} \nabla \cdot \hat{\mathbf{u}} - \frac{3}{\hat{c}} \cdot \nabla \hat{c} + \frac{1}{\hat{p}} \hat{\mathbf{u}} \cdot \nabla \hat{p} & \frac{\hat{c}}{\hat{p}\sqrt{\gamma}} (\nabla \hat{p})^T - \frac{2}{\sqrt{\gamma}} (\nabla \hat{c})^T & 0 \\ -\frac{1}{\sqrt{\gamma}} \nabla \hat{c} & \nabla \hat{\mathbf{u}} & \sqrt{\frac{\gamma-1}{\gamma}} (\frac{\hat{c}}{\hat{p}} \nabla \hat{p} - \nabla \hat{c}) \\ \sqrt{\gamma-1} \nabla \cdot \hat{\mathbf{u}} + \frac{2}{\hat{c}\sqrt{\gamma-1}} \hat{\mathbf{u}} \cdot \nabla \hat{c} & \frac{2}{\sqrt{\gamma(\gamma-1)}} (\nabla \hat{c})^T & \gamma \nabla \cdot \hat{\mathbf{u}} - \frac{1}{\hat{c}} \hat{\mathbf{u}} \cdot \nabla \hat{c} + \frac{1}{\hat{p}} \hat{\mathbf{u}} \cdot \nabla \hat{p} \end{pmatrix}. \tag{5}$$

To obtain an energy estimate, the symmetrized linearized Euler equations (1) are in turn written on split form scaled by density

$$\mathbf{q}_t + \frac{1}{2}[A\partial_1 \mathbf{q} + B\partial_2 \mathbf{q}] + \frac{1}{2\hat{\rho}}[\partial_1(\hat{\rho} A \mathbf{q}) + \partial_2(\hat{\rho} B \mathbf{q})] + H\mathbf{q} = \mathbf{f}. \tag{6}$$

Here, the matrix of the zeroth order term H satisfies

$$H = E - \frac{1}{2\rho}(\partial_1(\hat{\rho} A) + \partial_2(\hat{\rho} B)). \tag{7}$$

If topographic interfaces are presented in the domain, we imposed the rigid boundary condition on the boundary

$$\mathbf{u} \cdot \mathbf{n} = 0, \tag{8}$$

$$\hat{\mathbf{u}} \cdot \mathbf{n} = 0, \tag{9}$$

where $\mathbf{n}$ is the normal vector to the boundary. That is, the acoustic particle velocity and background flow vanish in the direction normal to the interface.

We discretize the equation (6) in space using sixth order finite-difference stencils away from the boundary and third order SBP operators [*Strand*, 1994] near the boundary. Readers are referred to *Petersson and Sjogreen* [2016] for the derivation of the energy estimates and SBP operators for the equation (6).

2.2. Transformation to curvilinear coordinates

In the previous subsection, the governing equation (6) is presented in Cartesian coordinates. For atmospheric sound propagation, it is well known that topographic boundary has significant influences on the sound propagation [*Lacanna et al.*, 2014; *Kim and Lees*, 2015]. In Cartesian coordinates non-planar boundaries can only be represented by staircase approximation. Each stairstep acts as a point scatterer producing high-frequency waves that may not be resolved by the finite-difference scheme. Very fine grids are required to remove the spurious scattering. In this section, we transform the equation (6) to the curvilinear coordinate that follows the topographic boundary [*Appelo and Petersson*, 2009; *Petersson and Sjogreen*, 2015, 2016]. This way complex, non-planar interfaces are readily modeled without the staircase approximation.

We start by developing a curvilinear formulation for the governing equation (6) following the approach in *Petersson and Sjogreen* [2016]. Assume that there is a one-to-one forward mapping,

$$\mathbf{x}(\mathbf{r}) = (x_1(\mathbf{r}), x_2(\mathbf{r}))^T, \mathbf{r} = (r_1, r_2)^T, \tag{10}$$

in the acoustic domain. By the chain rule we have the relations

$$\tilde{\partial}_q = \sum_{p=1}^{2} \frac{\partial x_p}{\partial r_q} \partial_p, \quad q = 1, 2, \quad \partial_i = \sum_{j=1}^{2} \frac{\partial r_j}{\partial x_i} \tilde{\partial}_j, \quad i = 1, 2, \tag{11}$$

where partial differentiation with respect to the curvilinear coordinates is denoted by $\hat{\partial}_k = \partial/\partial_{r_k}$. The derivatives of the forward and inverse mapping functions define the covariant and contravariant base vectors [*Thompson et al.*, 1985],

$$\mathbf{a}_k := \tilde{\partial}_k \mathbf{x} = \begin{pmatrix} \partial x_1/\partial r_k \\ \partial x_2/\partial r_k \end{pmatrix}, \quad \mathbf{a}^k := \nabla r_k = \begin{pmatrix} \partial r_k/\partial x_1 \\ \partial r_k/\partial x_2 \end{pmatrix}, \quad k = 1, 2. \tag{12}$$

By using the relations (11) and (12), the linearized Euler equations (6) can be transformed to curvilinear coordinates

$$\mathbf{q}_t + \frac{1}{2J}\left[\tilde{A}\tilde{\partial}_1 \mathbf{q} + \tilde{B}\tilde{\partial}_2 \mathbf{q}\right] + \frac{1}{2J\hat{\rho}}\left[\tilde{\partial}_1(\hat{\rho}\tilde{A}\mathbf{q}) + \tilde{\partial}_2(\hat{\rho}\tilde{B}\mathbf{q})\right] + H\mathbf{q} = \mathbf{f}. \tag{13}$$

Here, the transformed matrix $\tilde{A}$ and $\tilde{B}$ can be expressed in terms of the contravariant base vectors $\mathbf{a}^k = (\alpha_1^k, \alpha_2^K)^T$,

$$\tilde{A} = J(\alpha_1^1 A + \alpha_2^1 B), \tag{14}$$

$$\tilde{B} = J(\alpha_1^2 A + \alpha_2^2 B). \tag{15}$$

The Jacobian of the forward mapping function is obtained by

$$J = \det(\mathbf{a}_1 \ \mathbf{a}_2). \tag{16}$$

The rigid boundary condition is imposed along $r_2 = 0$ satisfying the conditions (8) and (9). The unit normal is represented by the contravariant base vectors along $r_2 = 0$

$$\mathbf{n} = \frac{1}{|\mathbf{a}^2|} \begin{pmatrix} \alpha_1^2 \\ \alpha_2^2 \end{pmatrix}. \tag{17}$$

Note that the boundary $r_2 = 0$ is alway flat in the parameter domain as the coordinate mapping functions (10) are determined to follow topographic interfaces.

The semi-discrete problem (13) is integrated in time by the classical 4th order explicit Runge-Kutta method, and the computational domain is truncated using the super-grid far-field technique [*Appelo and Colonius*, 2009].

3. Numerical examples

In this section we prove the accuracy and the correctness of the developed code by using the method of manufactured solution, and demonstrate its capabilities to solve practical acoustic problems that often arise in atmospheric acoustics.

3.1. Method of manufactured solution

The method of manufactured solution is a powerful technique to verify the correctness of the implementation of numerical algorithms. We start by defining the manufactured solution in a domain of $x_{max} = y_{max} = 1$ as

$$\rho = \sin(6.2(x - 1.3t)) \sin(6.2y), \tag{18}$$
$$u = \cos(6.2(x - 1.2t)) \sin(6.2y), \tag{19}$$
$$v = \cos(6.2(x - 1.1t)) \sin(6.2y), \tag{20}$$
$$p = \cos(6.2(x - t)) \sin(6.2y). \tag{21}$$

The parameters for the background condition are defined to be

$$\hat{\rho} = 1 + 0.2 \cos(w_m x + \phi_m) \sin(w_m y), \tag{22}$$
$$\hat{c} = 340 - 30 \sin(w_m x + \phi_m) \cos(w_m y + \phi_m), \tag{23}$$
$$\hat{u} = 10 \sin(w_m x) \cos(w_m y), \tag{24}$$
$$\hat{v} = 5 \sin(w_m x + \phi_m) \cos(w_m y), \tag{25}$$

where $w_m = 0.021$ and $\phi_m = 0.17$. And then the force term $\mathbf{f}$ in the equation (6) is determined such that the manufactured solution and background parameters satisfy the governing equation (6). On the boundaries at $x = 0, x = 1, y = 0$, and $y = 1$, homogeneous Dirichlet boundary conditions are imposed, which satisfy the manufactured solution.

Figure 1a) illustrates the initial condition of the manufactured overpressure at $t = 0$s. The numerical solutions are computed up to the time $t = 0.5$s and shown in Figure 1b).

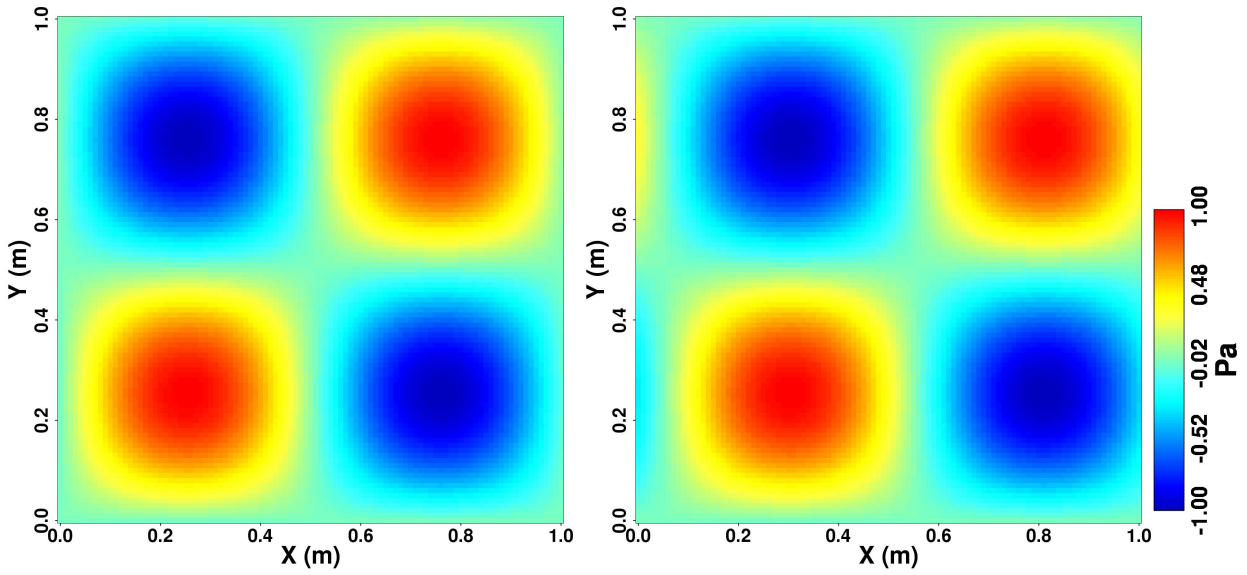

Figure 1: a) The manufactured solution for overpressure p at time $t = 0s$. b) The numerical overpressure computed at $t = 0.5s$.

h	$\|\|E\|\|_\infty$	$\|\|E\|\|_2$	p_∞	p_2
0.02	1.54×10^-4	1.63×10^-4	·	·
0.01	9.10×10^-6	8.56×10^-6	4.08	4.2
0.005	6.64×10^-7	4.87×10^-7	3.7	4.1
0.0025	4.17×10^-8	3.00×10^-8	3.9	4.02

Table 1: Maximum norm ($||E||_\infty$) and L^2 norm ($||E||_2$) errors for overpressure solution under grid refinement (h). The convergence rate is calculated as $\log_2 ||E||_{2h}/||E||_h$.

Table 1 displays the convergence rate of overepressue solution under grid refinement. The convergence rates in maximum norm (p_∞) and L^2 norm (p_2) at the final time shows forth order convergence, which is expected from the combination of sixth order accuracy in the interior domain and third order truncation errors in the SBP boundary closures.

3.2. Wave propagation in a uniformly moving medium

When a medium is homogeneous and moving in a uniform velocity, the linearized Euler equation can be reduced for overpressure p and particle velocity $\hat{\mathbf{u}}$ following the approach in *Ostashev et al.* [2005] as

$$\frac{\partial p}{\partial t} + \hat{\mathbf{u}} \cdot \nabla p + \hat{\rho}\hat{c}^2 \nabla \cdot \mathbf{u} = \hat{\rho}\hat{c}^2 F, \tag{26}$$

$$\frac{\partial \mathbf{u}}{\partial t} + \hat{\mathbf{u}} \cdot \nabla \mathbf{u} + \frac{\nabla p}{\hat{\rho}} = 0, \tag{27}$$

where F is the source term. We define the source to be a harmonic function

$$F = \frac{2iA}{\hat{\rho} w} e^{-iwt} \delta(x)\delta(y). \tag{28}$$

Assuming $|\mathbf{u}| < \hat{c}$ and $kr \gg 1$ where k is the wavenumber vector and r is the source-receiver distance, the asymptotic solution for overpressure can be obtained by following *Ostashev et al.* [2005]

$$p(r, \alpha, M) = \frac{A(\sqrt{(}1 - M^2 \sin^2\alpha) - M\cos\alpha)}{\sqrt{2\pi kr}(1-M^2)(1-M^2\sin^2\alpha)^(3/4)} \exp\left[\frac{i(\sqrt{(}1 - M^2\sin^2\alpha) - M\cos\alpha)kr}{1-M^2} + \frac{i\pi}{4}\right]. \tag{29}$$

Here, $M = |\hat{\mathbf{u}}|/\hat{c}$ is the Mach number and α is the angle between the downwind direction and the source-receiver direction.

Now we will compare the finite-difference modeling results with the analytic solution in the equation (29). The Dirac distribution in (28) is discretized to 6th order accuracy satisfying the six moment and six smoothness conditions [*Petersson et al.*, 2016]. In order to produce monochromatic harmonic wavefields, a finite-duration harmonic source time function tapered by a cosine function [*Ostashev et al.*, 2005] is used.

$$g(t) = \cos(2\pi f t + \phi) \times \begin{cases} (1/2)[1 - \cos(\pi t/T_1)], & 0 \le t < T_1, \\ 1, & T_1 \le t \le T - T_2, \\ (1/2)[1 - \cos(\pi(t-T)/T_2)], & T - T_2 < t \le T, \\ 0, & T < t, \end{cases} \tag{30}$$

where f is the source frequency and ϕ is the phase. T_1 and T_2 are the durations of the initiation taper and the termination taper, respectively. The cosine tapering is required to remove high frequency modes that can be generated by an abrupt change of the source time function in the beginning and the end. T is the total duration of source signal.

Figure 2 and 3 show the acoustic wavefields excited by the harmonic source located at $x = 60$m and $y = 60$m. We used the source parameters of $f = 100$Hz, $\phi = 0$, $T_1 = T_2 = 8/f$, and $T = 20/f$ for the equation (30). Note that the spectral properties of the source time function depend on the tapered cosine function that has a finite duration in the frequency domain [*Harris et al.*, 1978]. Given the above parameters, the Fourier transform of the source time function shows the peak amplitude at 100Hz. The amplitudes in the frequency domain decrease rapidly away from the peak frequency and fall below 5% of the peak amplitude at 113Hz which can be the highest effective frequency of the source time function. The speed of sound and ambient density of the medium is 340m/s and 1.22kg/m^3, respectively. The moving speed of the medium is different for Figure 2 and 3: the Mach number $M = 0.3$ for Figure 2 and $M = 0.6$ for Figure 3. The medium flows in the positive x direction, and the wavefields are recorded at $t = 0.24$s. Both wavefields show directional propagation characteristics of faster travel in the downwind direction (positive x) and high overpressure amplitudes in the upwind direction (negative x).

Figure 4 illustrates azimuth-dependent peak overpressure propagation with respect to different mesh sizes and medium Mach numbers. *Ostashev et al.* [2005] reported that the

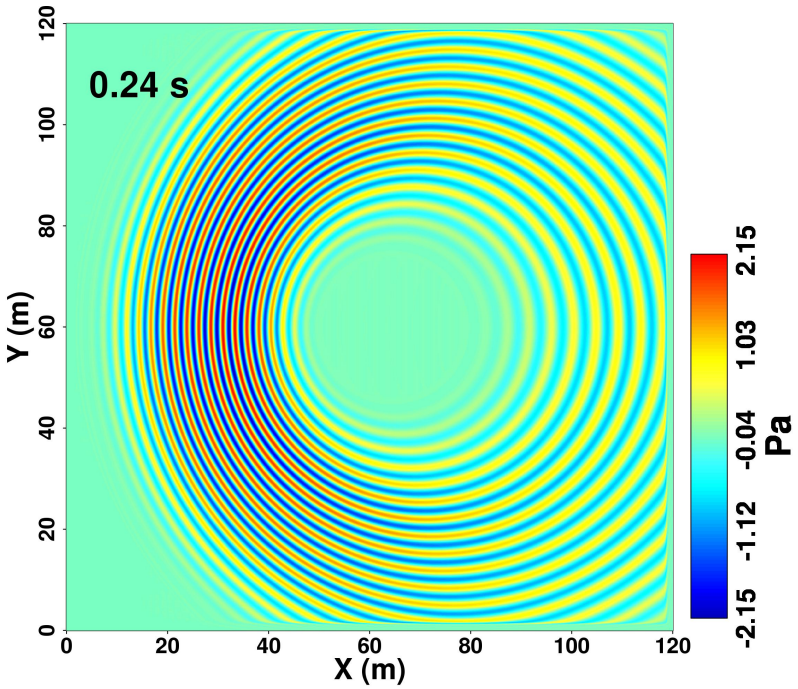

Figure 2: Acoustic wavefields excited by a finite-duration cosine function with a frequency of 100Hz. The acoustic waves propagate through the medium uniformly moving from the negative x direction to the positive x at the speed of the Mach number $M = 0.3$. The grid size is $h = 0.1$m.

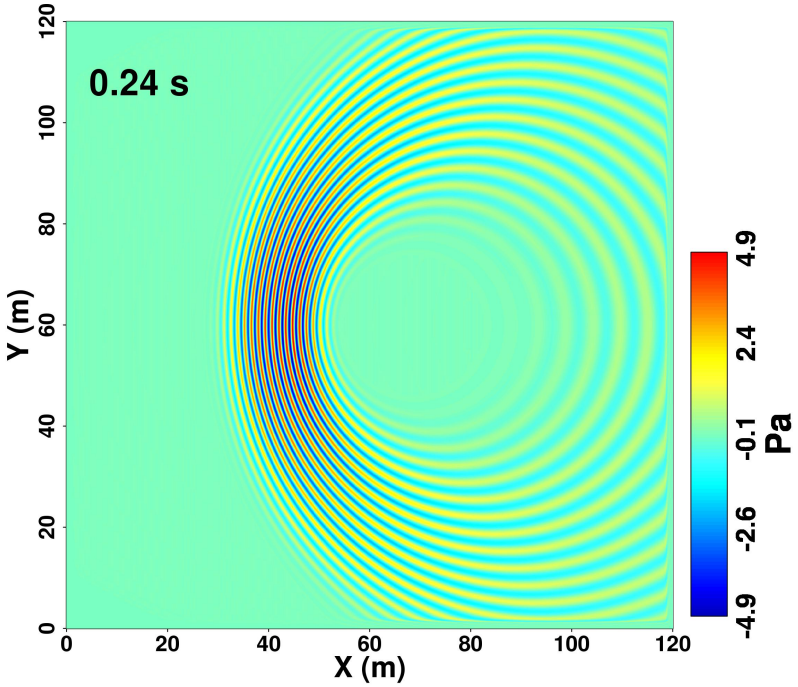

Figure 3: Acoustic wave propagation is simulated with the same parameters used in Figure 2 except for the medium speed of $M = 0.6$. With the high Mach number, wavefront steepening in the upwind direction (-x) and broadening in the downwind direction ($+x$) are pronounced.

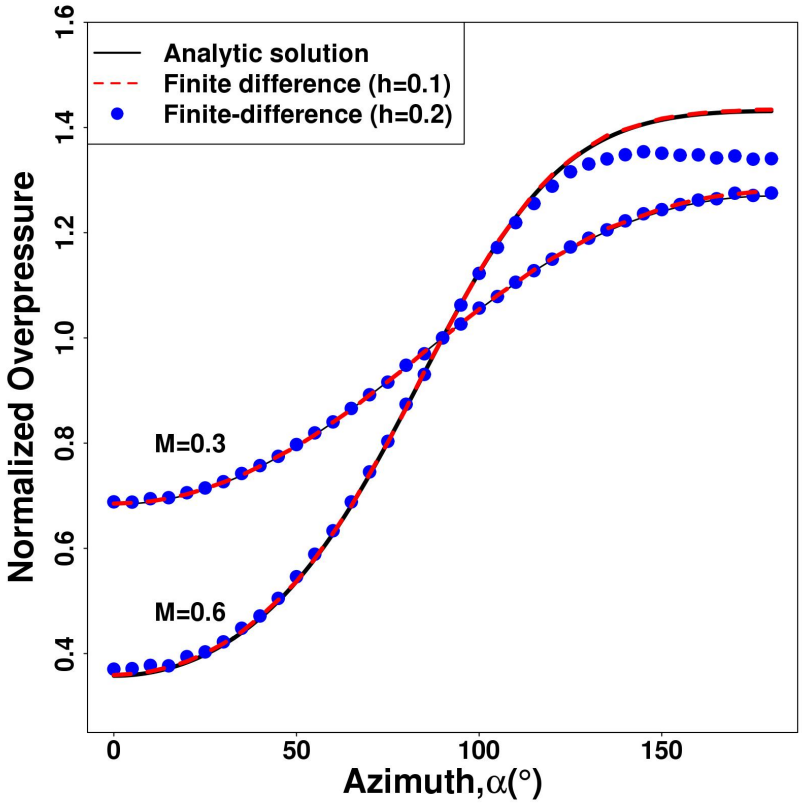

Figure 4: Azimuthal dependency of peak overpressure propagating in the moving medium. The theoretical solution (black line) of $|p(r, \alpha, M)/p(r, 90^o, M)|$ is calculated by the equation (29) for $M = 0.3$ and $M = 0.6$. Finite-difference simulations are performed with two different grid sizes h. The blue circles indicate the finite-difference calculations using $h = 0.2$m and the red dashed line indicates $h = 0.1$ m. The fine-grid numerical calculation shows good agreement with the analytic solution, but the coarse-grid finite-difference does not resolve sound propagations in the upward direction ($\alpha = 180^o$). See the text for details.

asymptotic solution showed good agreement with numerical solutions when $kr \geq 10$. We recorded finite-difference peak overpressures and calculated $|p(r, \alpha, M)/p(r, 90^o, M)|$ at $r =$ 25m and $0^o \leq \alpha \leq 180^o$ for $M = 0.3$ and 0.6, where $kr \simeq 46$ and $\alpha = 0$ corresponds to the downwind direction $(+x)$. In Figure 4, the blue circles are the finite-difference calculation for the grid interval of $h = 0.2$m, and the red dashed line results from $h = 0.1$m. For the low Mach number $M = 0.3$ both grid sizes modeled the acoustic waves well showing good agreement with the analytic solution. However, for the high Mach number $M = 0.6$ the coarse grid case could not resolve the wave propagation especially in the upwind direction $(-x)$. This result may be explained by apparent sound speed. When sound waves travel through a moving medium, their propagation speed, called the effective speed of sound $(\hat{c}_{eff})$, is affected by the moving velocity of the medium [*Godin*, 2002] as

$$\hat{c}_{eff} = \hat{c} + \hat{\mathbf{u}} \cdot \mathbf{r}, \tag{31}$$

where $\mathbf{r}$ is a unit vector in the direction of sound propagation. The effective sound speed in the upwind direction for $M = 0.6$ in Figure 4 is 136 m/s, and in this case, the effective wavelength for 113 Hz is ~ 1.2m. The grid size $h = 0.2$m corresponds to only ~ 6 points per the shortest wavelength, which does not meet the minimum requirement of grid points. Therefore, the upwind waves in $M = 0.6$ is not well resolved by the given grid interval. However, the fine grid interval $h = 0.1$m corresponds to ~ 12 grid points per the wavelength and provide a numerical solution with good accuracy.

3.3. Acoustic point source

A "point" source in the 2-D domain does not excite spherical waves, rather it creates cylindrical waves radiating from an infinite line that is normal to the 2-D plane. Amplitudes of the cylindrical waves decay inversely proportional to the square root of normal distance to the line source, instead of the inverse distance of the spherical spreading. Modeling capability of a point source and spherical propagation of acoustic waves is often required to solve geophysical problems as many natural and/or man-made explosions are modeled as a point source. In addition, the spherical spreading of wavefields must be taken into account to obtain accurate transmission energy loss of sound waves in the atmosphere.

In this subsection, we investigate the conversion of 2D acoustic signals into 3D signals. The 3D solution approximation by 2D solutions have been explored by many authors in seismology [*Helmberger and Vidale*, 1988; *Miksat et al.*, 2008; *Xiong et al.*, 2013; *Li et al.*, 2014]. Assuming homogeneous whole space, 3D acoustic signals p_{3D} from a point source [*Li et al.*, 2014] can be written in terms of 2D acoustic signals p_{2D} from a line source

$$p_{3D}(x, y, 0, t) = \frac{1}{\pi} \sqrt{\frac{\alpha}{2x}} \frac{d}{dt} \left[\frac{1}{\sqrt{t}} * p_{2D}(x, y, t) \right], \tag{32}$$

where $\alpha = x/(2\hat{c})$ is the geometric ray parameter.

We create a 2-D overpressure signal using an impulsive source time function shown in Figure 5. Figure 6 shows the resultant cylindrical wavefields propagating in a non-moving

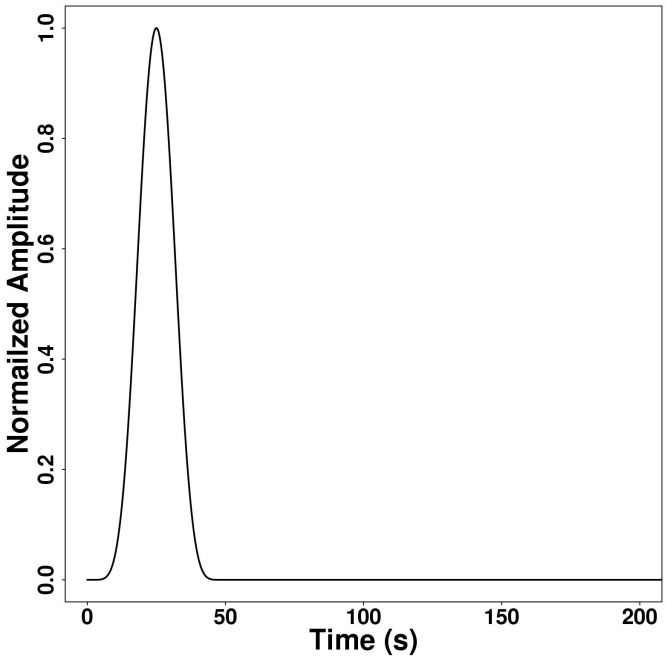

Figure 5: An impulsive source time function used to create 2-D cylindrical waves.

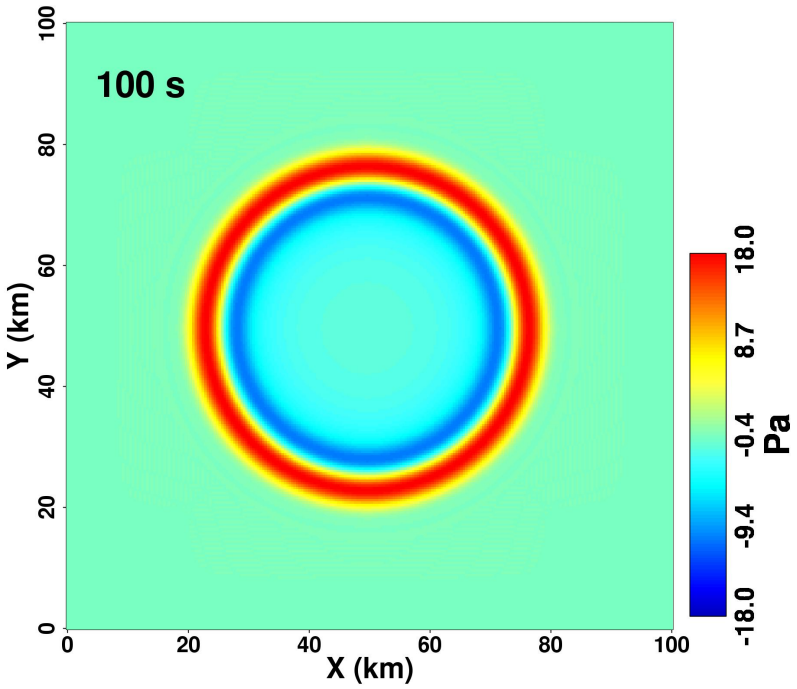

Figure 6: Cylindrical acoustic waves excited by the source time function in Figure 5.

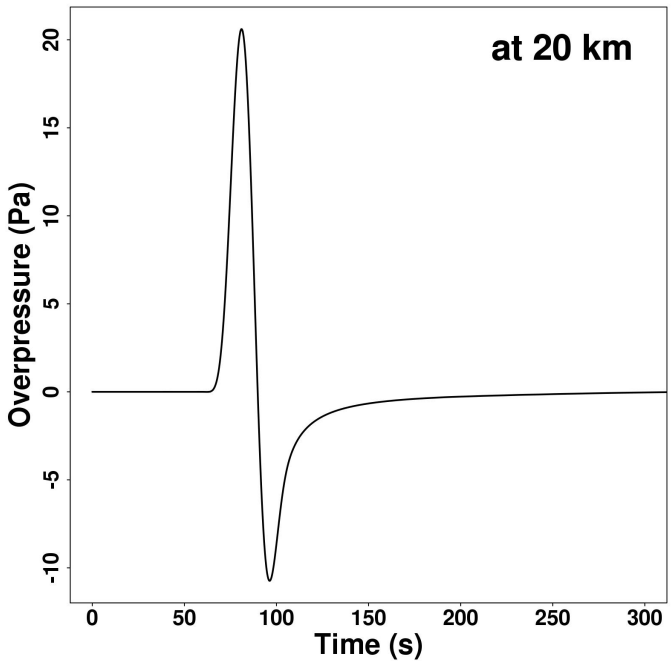

Figure 7: The 2-D acoustic overpressure measured at 20 km from the source. Due to the contribution from the infinite line source, the cylindrical waves have a long tail following the first pulse.

homogeneous whole space with the speed of sound $\hat{c} = 340$m/s. An overpressure signal measured at 20 km away from the source is shown in Figure 7. As each part of the infinite line source contributes the resultant waveform at different time, 2-D cylindrical waves typically have a long negative tail following the initial positive pressure. We apply the conversion equation (29) to the 2-D overpressure signals. The convolution operation is performed numerically. As the accuracy of the numerical convolution strongly depends on the time resolution of the 2-D signals, we integrate the equation (6) in time with a fine time step of $dt = 0.1$s that corresponds to the Courant number of 0.1 (note that Courant number of 1.0 typically ensures the stability, which corresponds to $dt = 1.0$ s in this case.)

Figure 8 and 9 shows the converted 3-D acoustic overpressures at 20 km and 30 km from the source. Theoretical 3-D solutions at the same positions are calculated using the source time function in Figure 7. The converted 3-D acoustic signals fit the pure 3-D signals reasonably well. This waveform agreement also suggests that our numerical 2-D solutions are accurate indicating the correctness of the line source implementation. There are small misfits between them, which is probably caused by the error of numerical convolution. Finer temporal resolution for the 2-D signal can improve the accuracy of the 3-D conversion. In addition, now the amplitudes of the converted 3-D signals decay following the inverse distance law, which allows for the computation of sound transmission loss in spherical spreading using 2-D modeling.

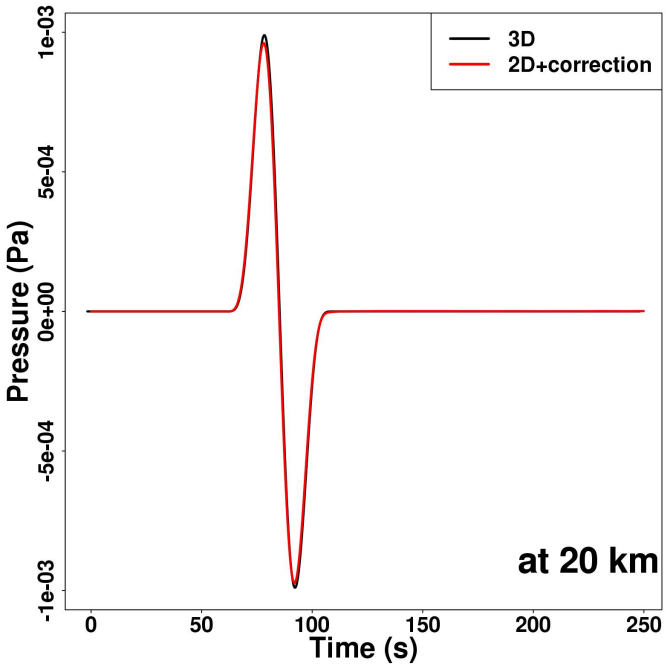

Figure 8: The converted 3-D acoustic overpressure (red line) and theoretical 3-D solution (black line) at 20 km from the source. Two signals show reasonably good agreement. The converted 3-D signal slightly underestimates the peak amplitudes, which may be caused by the error of numerical convolution for the equation (29).

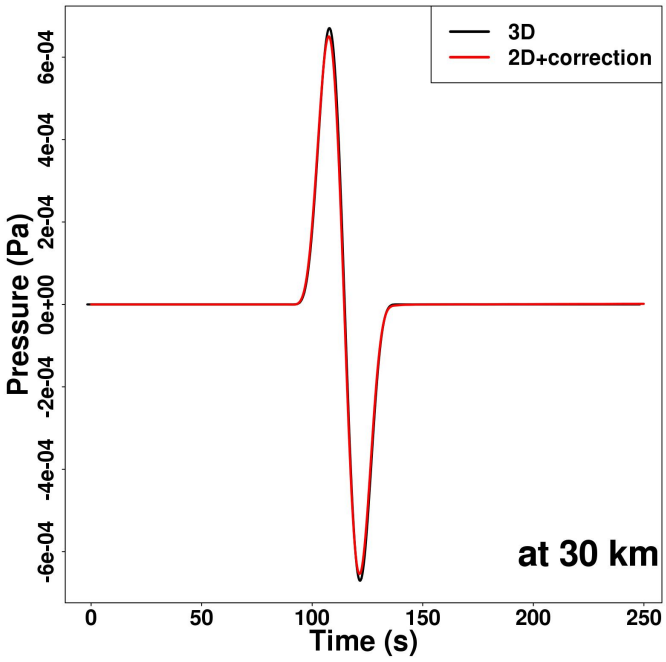

Figure 9: The converted (red) and theoretical (black) 3-D acoustic signals are compared at a distance of 30 km. They show the similar results to Figure 8, which indicate the converted signals follow the inverse distance spreading law.

We briefly explored the applicability of 2-D modeling to approximate 3-D point-source solution in a simple case. For a general 2-D media, a similar conversion to 3-D signals are possible but requires the integration of wave travelling speed along the entire ray path [*Cerveny*, 2005], which is beyond the scope of this report.

4. Summary

We developed a 2-D acoustic solver using finite-difference operators that satisfy the summation-by-parts principle. The 2-D algorithm substantially reduces computational workload for the finite-difference calculation, and hence can be used to simulate long-range sound propagation in the atmosphere and to study high-frequency sound waves, where full 3-D waveform simulation may be too onerous. We verified the accuracy and correctness of numerical implementation using the method of manufactured solutions and several numerical experiments. In addition, approximation of 3-D solution by 2-D modelings was discussed for a simple case. For a homogeneous whole space, 2-to-3D conversion of signal showed promising results to predict overpressure amplitudes of spherical spreading waves using 2-D simulation. However, further study will be required to extend the conversion technique for more general case.

Acknowledgments

The 2-D acoustic code was developed with support from LLNL Laboratory Directed Research and Development project 14-ER-001. This work was performed under the auspices of the U.S. Department of Energy by Lawrence Livermore National Laboratory under Contract DE-AC52-07NA27344.

References

Appelo, D., and T. Colonius (2009), A high-order super-grid-scale absorbing layer and its application to linear hyperbolic systems, *Journal of Computational Physics*, *228*(11), 4200 – 4217, doi:http://dx.doi.org/10.1016/j.jcp.2009.02.030.

Appelo, D., and N. A. Petersson (2009), A stable finite difference method for the elastic wave equation on complex geometries with free surfaces, *Communications in Computational Physics*, *5*(1), 84 – 107.

Bonner, J. L., D. R. Russell, and R. E. Reinke (2013), Modeling surface waves from above-ground and underground explosions in alluvium and limestone, *Bulletin of the Seismological Society of America*, doi:10.1785/0120130069.

Cerveny, V. (2005), *Seismic ray theory*, Cambridge university press.

Ford, S. R., A. J. Rodgers, H. Xu, D. C. Templeton, P. Harben, W. Foxall, and R. E. Reinke (2014), Partitioning of seismoacoustic energy and estimation of yield and heightof-

burst/depthofburial for nearsurface explosions, *Bulletin of the Seismological Society of America*, doi:10.1785/0120130130.

Gainville, O., P. Blanc-Benon, E. Blanc, R. Roche, C. Millet, F. L. Piver, B. Despres, and P. F. Piserchia (2009), *Misty Picture: A Unique Experiment for the Interpretation of the Infrasound Propagation from Large Explosive Sources*, pp. 575–598, Springer Netherlands, Dordrecht, doi:10.1007/978-1-4020-9508-5_18.

Godin, O. A. (2002), An effective quiescent medium for sound propagating through an inhomogeneous, moving fluid, *The Journal of the Acoustical Society of America*, *112*(4), 1269–1275, doi:http://dx.doi.org/10.1121/1.1504853.

Harris, F., et al. (1978), On the use of windows for harmonic analysis with the discrete fourier transform, *Proc. IEEE*, *66*(1), 51–83.

Helmberger, D. V., and J. E. Vidale (1988), Modeling strong motions produced by earthquakes with two-dimensional numerical codes, *Bulletin of the Seismological Society of America*, *78*(1), 109–121.

Kim, K., and J. M. Lees (2014), Local volcano infrasound and source localization investigated by 3d simulation, *Seismological Research Letters*, *85*(6), 1177–1186, doi:10.1785/0220140029.

Kim, K., and J. M. Lees (2015), Imaging volcanic infrasound sources using time reversal mirror algorithm, *Geophysical Journal International*, *202*(3), 1663–1676, doi:10.1093/gji/ggv237.

Kim, K., and A. Rodgers (2016), Waveform inversion of acoustic waves for explosion yield estimation, *Geophysical Research Letters*, *43*(13), 6883–6890, doi:10.1002/2016GL069624, 2016GL069624.

Lacanna, G., M. Ichihara, M. Iwakuni, M. Takeo, M. Iguchi, and M. Ripepe (2014), Influence of atmospheric structure and topography on infrasonic wave propagation, *Journal of Geophysical Research: Solid Earth*, *119*(4), 2988–3005, doi:10.1002/2013JB010827.

Li, D., D. Helmberger, R. W. Clayton, and D. Sun (2014), Global synthetic seismograms using a 2-d finite-difference method, *Geophysical Journal International*, *197*(2), 1166–1183, doi:10.1093/gji/ggu050.

Miksat, J., T. M. Mller, and F. Wenzel (2008), Simulating three-dimensional seismograms in 2.5-dimensional structures by combining two-dimensional finite difference modelling and ray tracing, *Geophysical Journal International*, *174*(1), 309–315, doi:10.1111/j.1365-246X.2008.03800.x.

NOAA, N. (1976), USAF. US Standard Atmosphere, 1976, *US Government Printing Office, Washington, DC, USA*.

Ostashev, V., D. Wilson, L. Liu, D. Aldridge, N. Symons, and D. Marlin (2005), Equations for finite-difference, time-domain simulation of sound propagation in moving inhomogeneous media and numerical implementation, *The Journal of the Acoustical Society of America*, *117*, 503, doi:10.1121/1.1841531.

Park, J., S. J. Arrowsmith, C. Hayward, B. W. Stump, and P. Blom (2014), Automatic infrasound detection and location of sources in the western United States, *Journal of Geophysical Research: Atmospheres*, doi:10.1002/2013JD021084.

Petersson, N. A., and B. Sjogreen (2015), Wave propagation in anisotropic elastic materials and curvilinear coordinates using a summation-by-parts finite difference method, *Journal of Computational Physics*, *299*, 820 – 841, doi:http://dx.doi.org/10.1016/j.jcp.2015.07.023.

Petersson, N. A., and B. E. Sjogreen (2016), High order accurate finite difference modeling of seismoacoustic wave propagation in a moving atmosphere and a heterogeneous earth model coupled across a realistic topography, submitted to J. of Sci. Comput. (October 2016), LLNL-JRNL-704612.

Petersson, N. A., O. O'Reilly, B. E. Sjogreen, and S. Bydlon (2016), Discretizing singular point sources in hyperbolic wave propagation problems, *Journal of Computational Physics*, *321*, 532 – 555, doi:http://dx.doi.org/10.1016/j.jcp.2016.05.060.

Sjogreen, B. E., and N. A. Petersson (2016), User's guide to elac, version 1.0, Lawrence Livermore National Laboratory, Technical report LLNL-SM-704300 (2016).

Strand, B. (1994), Summation by parts for finite difference approximations for d/dx, *Journal of Computational Physics*, *110*(1), 47 – 67, doi:http://dx.doi.org/10.1006/jcph.1994.1005.

Thompson, J. F., Z. U. Warsi, and C. W. Mastin (1985), *Numerical grid generation: foundations and applications*, vol. 45, North-holland Amsterdam.

Walker, K. T., R. Shelby, M. A. H. Hedlin, C. de Groot-Hedlin, and F. Vernon (2011), Western U.S. Infrasonic Catalog: Illuminating infrasonic hot spots with the USArray, *Journal of Geophysical Research: Solid Earth*, *116*(B12), doi:10.1029/2011JB008579.

Xiong, J. L., Y. Lin, A. Abubakar, and T. M. Habashy (2013), 2.5-d forward and inverse modelling of full-waveform elastic seismic survey, *Geophysical Journal International*, *193*(2), 938–948, doi:10.1093/gji/ggt013.